Supporting Material
Coupling controls synchrony of clock cells in development and knockouts

Isao T. Tokuda, Daisuke Ono, Bharath Ananthasubramaniam,
Sato Honma, Ken-Ichi Honma, Hanspeter Herzel

This supplementary material presents detailed numerical procedures for simulations of mathematical model of the cellular network model and analyses of experimental and simulation data. It contains ten sections: (1) amplitude-phase modeling of dispersed data, (2) network of coupled amplitude-phase models, (3) quantification of slice data, (4) Hopf bifurcation of the single cell model, (5) dependence of network dynamics on system parameters, (6) entrainment of network dynamics to external stimuli, (7) simulation of actograms, (8) analysis of slice culture data, (9) detailed parameter setting for the biochemical model, (10) additional samples of bioluminescence signals.

1 Amplitude-phase modeling of dispersed data

Taking two examples of dispersed cell culture data (one from wild-type and the other from knockout mouse), this section provides basic procedures of fitting the amplitude equation model to the experimental data. First, bioluminescence signal $\{x(t) : t = 1, 2, \ldots, T\}$ recorded from dispersed cell of neonate SCN slice was detrended using a least square fitting of a second-degree polynomial. The polynomial was subtracted from the signal so that the signal was mean centered. The detrended signal was the normalized in such a way that the signal has zero mean and unit variance. Figs. S1, *a* and *d*, represent detrended and normalized signals from the raw data of Fig. 1, *a* and *d*, respectively.

Second, with respect to the normalized signal $x(t)$, the autocorrelation $C(k)$ (with the time lag of k sampling intervals) was computed as

$$C(k) = \frac{1}{M-k}\sum_{i=1}^{M-k}(x_i - \bar{x}_0)(x_{i+k} - \bar{x}_k) \tag{S1}$$

where M is the number of samples in the time-series, and $\bar{x}_0 = \frac{1}{M}\sum_{i=1}^{M} x_i$ and $\bar{x}_k = \frac{1}{M-k}\sum_{i=1}^{M-k} x_{i+k}$ represent the mean values. The autocorrelation function detects periodicity in the signal $x(t)$, where the time lag that points to the first peak roughly corresponds to the period length of the signal.

Third, parameters of the stochastic amplitude-phase model of Eq. 1 were estimated by fitting the model to the experimental data. The single cell model has five unknown parameters $\{A, \omega, \lambda, D_r, D_\varphi\}$ to be fitted to the dispersed cell culture data. As described in the main text, the single cell model has an autocorrelation function defined by Eq. 3. The five parameters were optimized so that the autocorrelation function of the single cell model is fitted to that of the bioluminescence signal. We used `lsqcurvefit` subroutine of the MATLAB Statistical Toolbox to optimize the parameters. It should be noted that the fitting of Eq. 3 may face the problem of local minima, since the function involves a summation of two exponentials, which may create redundancy. To avoid missfitting, initial guesses were used as described in detail in [1]. Figs. S1, *c* and *f*, compare autocorrelation function $C(k)$ of the experimental data and that of the fitted model. The model captures basic feature of the experimental curve fairly well. From the estimated parameters, the intrinsic period and the coefficient of variation were obtained as $T = 2\pi/\omega$ and $\mathrm{CV} = \sigma_r/A = (\sqrt{D_r/\lambda})/A$. For the experimental data shown in Figs. 1, *a* and *d* (corresponding to Figs. S1, *a* and *d*), they were estimated as $T = 22.5$ h, CV = 1.3 for the wild-type cell and $T = 33.5$ h, CV = 3.2 for the knockout cell.

The same procedure was repeated for dispersed culture data of wild-type cells ($N = 74$) and $Cry1^{-/-}/Cry2^{-/-}$ cells ($N = 48$). $N = 66$ WT cells and $N = 14$ knockout cells were fitted to the model reasonably well. The results are summarized in Figs. 1, *c* and *f*, where estimated CV is plotted against estimated period $T = 2\pi/\omega$. Compared to the wild-type, the period was distributed more broadly in the knockoutm. As summarized in Table. 1, the mean and the standard deviation were 24.3±1.1 h for the wild-type and 31.1±7.3 h for the knockout. Of special note is that, if the CV is greater than 1, probability density of the state variables of the oscillator becomes qualitatively the same as that of a damped oscillator. However, if the CV is less than 1, it can be characetrized as a self-sustained oscillator. Hence, $CV = 1$ provides a criterion to distinguish self-sustained oscillators from damped oscillators. Among the wild-type cells, 36.4% of the neurons were characterized as self-sustained oscillators (textiti.e., $\mathrm{CV} < 1$), whereas no cell were classified into self-sustained oscillators in the knockout cells.

Finally, the effect of detrending on the data was examined. In the studies of circadian rhythms, the detrending has been widely utilized as a postprocessing of the measurement data. Since our method focuses on existence of a limit cycle oscillation around the origin, the signal detrending, which introduces changes to oscillation amplitude, may influence the results. Fig. S2 summarizes the results of single cell analysis without detrending of the data. Compared with Figs. 1, *c* and *f*, the overall structure remains the same. As anticipated, the CV range is slightly increased, because the trend component, which exists in the raw data and was not removed by the detrending, might have hidden the oscillatory structure in the signal amplitude. The estimated period was 24.2±1.1 h for the wild-type cells and 26.8±7.0 h for the knockout cells. Among the wild-type cells, 7.2% of the cells were characterized as self-sustained oscillators, whereas no cells were classified into self-sustained oscillators. Compared to the results with

detrended data, the period estimates remained almost the same. Concerning the percentile of the self-sustained oscillators, it decreased in the non-detrended WT data. This is becase large portion of the WT cells is located around the critical line (CV = 1) and the slight shift in CV moved the cells to region of noisy oscillators (textiti.e., CV > 1).

We consider that the effect of the detrending does not influence our conclusion, since essentially the same features remained to distinguish $Cry1^{-/-}/Cry2^{-/-}$ cells from wild-type cells. Alternative criterion, which is less sensitive to a small shift in CV, should be further developed to characterize self-sustained oscillators.

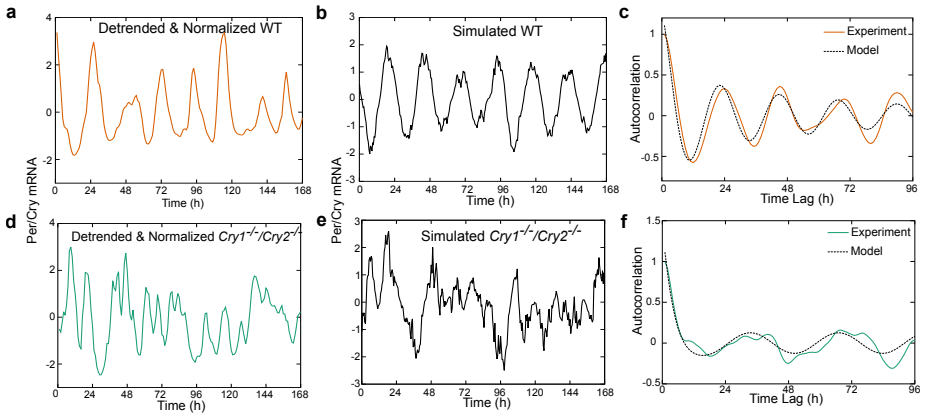

Figure S1: Procedure for parameter estimation. **a**, **d**: Detrended and normalized signals. **b**, **e**: Simulated signal by the stochastic amplitude model with estimated parameters. **c**, **f**: Autocorrelation functions of the experimental data (red solid line: WT, green solid line: knockout) and model (black dotted line).

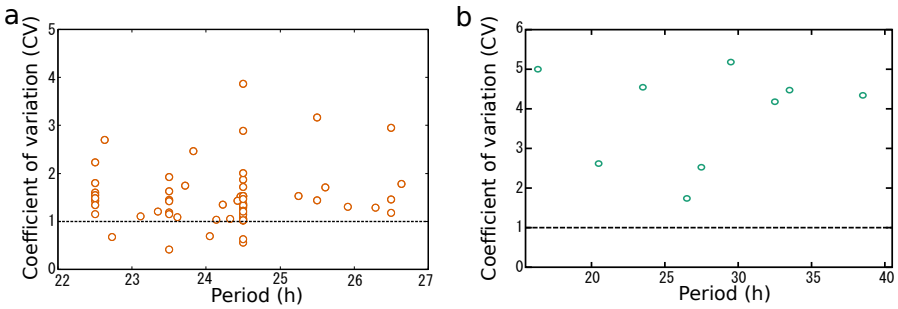

Figure S2: Single cell analyses of biolumninescence signals from dispersed cell culture without detrending. Abscissa and ordinate represent estimated period and coefficient of variation CV, respectively. (**a**): wild-type ($N = 69$). (**b**): knockout ($N = 10$).

2 Network of coupled amplitude-phase models

In this section, we construct a network of amplitude-phase models, each of which was fitted to dispersed cellular data in the previous section. By studying the network dynamics, we examine whether macroscopic properties such as dynamical characteristics of the slice data can be reproduced by the model. In particular, we focuse on the synchronization property of the cellular network.

The single cell model of the stochastic amplitude-phase equations 1-2 can be represented in Cartesian (x, y)-coordinates as

$$\frac{dx}{dt} = -\lambda\frac{x}{r}(r - A) + \omega y + \xi_x, \tag{S2}$$

$$\frac{dx}{dt} = -\lambda\frac{y}{r}(r - A) + \omega x + \xi_y, \tag{S3}$$

where ξ_x and ξ_y are independent Gaussian noises and $r = \sqrt{x^2 + y^2}$. By applying interneuronal connections though x and y variables, a network of SCN cells was constructed as Eqs. 4-5. The coupling is characterized by the strength K and delay ψ. From the data fitting detained in the previous section, we obtained N single cell models, whose parameters (λ_i, A_i, ω_i) correspond to the dispersed cellular data well. Such parameters were used to construct a network composed of $N = 66$ and $N = 14$ neurons for the wild-type and knockout mice, respectively.

Fig. 2 shows dependence of the network synchrony on the coupling strength K and coupling delay ψ. The level of synchrony was measured by the synchronization index $R = \frac{<\bar{x}^2> - <\bar{x}>^2}{\frac{1}{N}\sum_{i=1}^{N}(<x_i^2> - <x_i>^2)}$ as defined by Eq. 6. $< \cdots >$ denotes average over time and $\bar{X} = \frac{1}{N}\sum_{i=1}^{N} X_i$ is the average of x-variables among N oscillators. For the network of amplitude oscillators, whose parameter values were extracted from the WT cells (Fig. 2*a*), clear synchrony appears as the coupling strength is increased. Interestingly, the synchronization depends upon the coupling delay ψ. Although a small delay enhances the synchronization, a medium delay around $\psi = 12$ h destroys the synchronization. It has been known in coupled phase oscillators that the coupling force can be easily turned repulsive by a shift of half of the intrinsic period. The observed desynchrony can be understood as a result of such repulsive coupling. Similar structure can be observed in the synchronization diagram of the network constructed from knockout cells (Fig. 2*b*). Compared to the case of WT cells, the regime of synchronization is smaller. Moreover, the level of synchrony is not so high even with a strong coupling and a small coupling delay. This is due to the extended heterogeneity of the knockout cells, which require stronger coupling to induce global synchrony. Higher level of noise also disturbed the synchronized cellular activities.

For fixed coupling strength and delay, traces of the cellular activities coupled were drawn in Fig. S3. The simulated models capture essential features of the bioluminescence data of Fig. 5. Setting the coupling strength and delay as $K = 0.1$ and $\psi = 0$ h, default situation for neonate slice was established.

Under the default setting, networks of both WT and knockout cells generated synchronized cellular activities. Introduction of the delay of $\psi = 5.5$ h maintained the synchrony in the WT cells, whereas it destroyed the synchrony in the knockout cells. Such features closely resemble the adult slices of Figs. 5, *b* and *e*. To simulate the administration of tetrodotoxin (TTX), the coupling strength was reduced from $K = 0.1$ to $K = 0.04$ at time $t = 72$ h in Figs. S3, *c* and *f*. Whereas the WT cells maintained the synchronized oscillations even after the TTX, phases of the knockout cells started to get apart from each other, resulting in a desynchronized oscillations after the TTX. These reproduce qualitative features of the TTX experiment of Figs. 5, *c* and *f*, very well.

To summarize, the network of coupled amplitude equations simulated essential features of the experimental data. The coupling strength K and delay ψ may play a key role in organizing the slice activities as well as in inducing a developmental change from neonate to adult. This agrees with our results of network of biochemical models (Eqs. 7-18) composed of transcriptional/translational feedback loops of the core clock genes simulated in the main text. Our conclusion that variation of the three parameters (*i.e.*, individual oscillator characteristics, strength of coupling, and timing of coupling) suffices to reproduce experimental data is general, largely independent of the choice of the oscillator models.

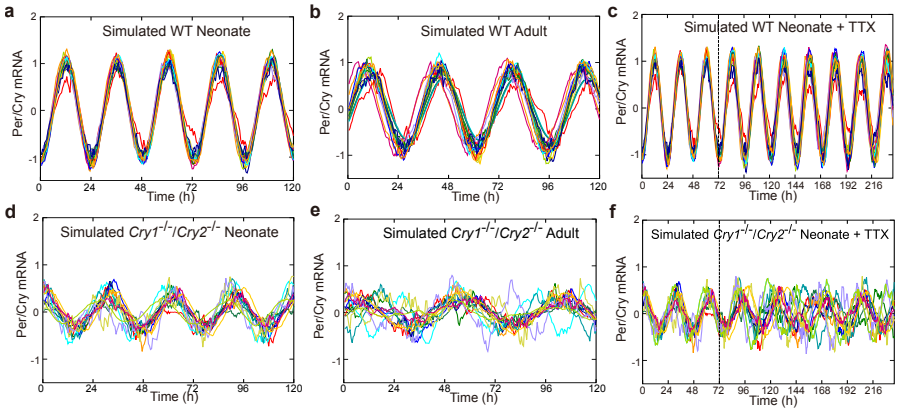

Figure S3: Simulation of coupled amplitude equation models corresponding to Fig. 5. **a,b,c**: Network of amplitude models constructed from wild-type (WT) SCN cells ($K = 0.1$). (**a,c**) and (**b**) represent neonates ($\psi = 0$), and adults ($\psi = 5.5$h), respectively. The dashed line in (**c**) indicates the time at which the coupling was lowered from $K = 0.1$ to $K = 0.04$ simulating administration of tetrodotoxin. **d,e,f**: Network of amplitude models constructed from $Cry1^{-/-}/Cry2^{-/-}$ mouse ($K = 0.1$). The neonate ($\psi = 0$) is shown in (**d,f**) and adults ($\psi = 5.5$h) in (**f**).

3 Quantification of slice data

The cultured SCN slice data from neonate and adult mice (both wild-type and knockout) were analyzed. First, cellular signals $\{x_i(t) : i = 1, 2, \ldots, N_c; t = 1, 2, \ldots, M\}$ were extracted from the regions of interest in the bioluminescence image (Fig. 5). The number of the cells and the data length were $(N_c, M) = (126, 155)$, $(87, 143)$, $(97, 136)$, $(63, 199)$ for neonate wild-type, adult wild-type, neonate knockout, and adult knockout mice, respectively. The extracted signals were then analyzed by the chi-square periodogram (significance level of 1 %) [2]. Average and standard deviation of the estimated periods were summarized in Table S1 (neonate wild-type: $N = 126$, adult wild-type: $N = 78$, neonate knockout: $N = 97$, adult knockout: $N = 22$).

To quantify the level of synchrony among cellular signals of the slice, the cellular phases were estimated by the Cosinor's method [3]. The phase ϕ_i of the i-th cell was determined by fitting a cosine function $a * \cos(2\pi(t + \phi_i)/\tau)$ to the cellular signal $\{x_i(t) : t = 40, 41, \ldots, 60\}$, where a is an oscillation amplitude and τ is the average period previously estimated. The phase estimate ϕ_i with the coefficient of determination larger than 0.5 was considered reliable. Standard deviation of the phases of individual cells, which measures the coherence structure, was summarized in Table S1 (neonate wild-type: $N = 126$, adult wild-type: $N = 66$, neonate knockout: $N = 97$, adult knockout: $N = 5$). Extended variations of the phase distributions in adult slices are observed in both experiment and model. The averaged periods are also in good agreement except those of the neonate knockout slice. Although the period is shortened in the experiment, it is elongated in the model. The elongated period of the model might be due to the coupling delay, which lengthened the feedback loops of individual cells. The cause of the shortened period observed in the experiment is not well understood.

4 Hopf bifurcation of the single cell model

To identify the transition from damped oscillations to self-sustained oscillations, a bifurcation diagram was drawn. In the single cell model of Eqs. 7-18, the parameter values P_1 generate self-sustained oscillations [4], whereas P_2 give rise to damped oscillations [5]. By changing the oscillator strength α ($0 \leq \alpha \leq 1$), which interpolates the two parameter sets as Eq. 19, local maximum of the Y_1 value was plotted in Fig. S4*a*. The onset of self-sustained oscillations was observed around $\alpha = 0.5$. To see the bifurcation type, the largest eigenvalue of the Jacobian matrix of the model was simultaneously computed and plotted in Fig. S4*b*. At the onset point, the real part of the eigenvalue, which is negative before the onset, touches the zero line, while the imaginary part exists, implying the Hopf bifurcation.

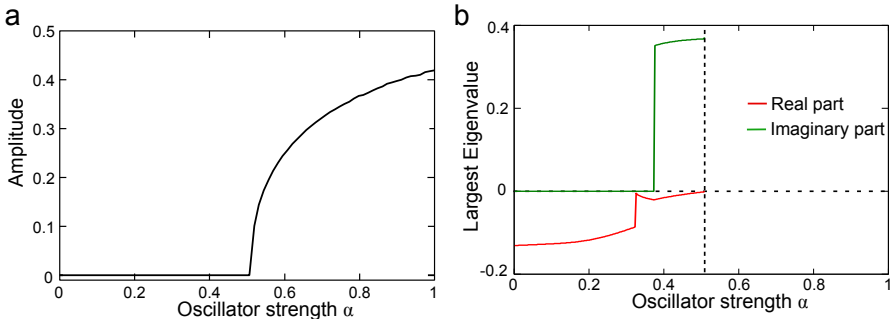

Figure S4: **a**: Dependence of the oscillation amplitude of the single cell model on oscillator strength α. **b**: Largest eigenvalue computed simultaneously with **a** from Jacobian matrix of the single cell model (red: real part, green: imaginary part). At oscillation onset around $\alpha = 0.5$, real part of the complex eigenvalue crosses the zero-line, implying Hopf bifurcation.

5 Dependence of network dynamics on system parameters

To study dependence of the network dynamics on system parameters, we systematically varied the single cell oscillator strength $\alpha \in [0, 1]$, the coupling strength $K \in [0, 1.5]$, and its delay $\psi \in [0, 24]$. The degree of synchrony was quantified by the synchronization index R defined by Eq. 6. In Fig. 6*a*, the delay was fixed to $\psi = 0$, while the other two parameters were varied. In Fig. 6*b*, the coupling strength was fixed to $K = 1$, while the other two parameters were varied. In Figs. S5, *a* and *b*, period length of the simulated network was drawn in 2-dimensional diagrams corresponding to Figs. 6, *a* and *b*. For each cell, the individual period was computed by the chi-square periodogram (significance level of 1 %) [2] and their periods were averaged to represent the network period.

As seen in the blue regions of Fig. S5, small oscillator strength ($\alpha < 0.5$) dampens rhythmicity and sets the network period to zero. The coupling strength K recovers the rhythmicity even in the region, where individual cells are damped oscillators (Fig. S5*a*). In this region, a clear synchronization among the neurons is observed (Fig. 6*a*). This agrees quite well with the earlier study that damped single cells are easy to synchronize with each other and that the synchronization recovers rhythmicity of the damped cells [6, 5]. Large coupling strength K increases the synchronization index further.

The timing of coupling described by ψ also has a very strong effect on synchronization. As indicated in Figs. 6*b* and S5*b*, a small change in ψ can easily destroy synchronization. Of particular note is the blue region of Fig. S5*b*, where the synchronization-induced rhythmicity was broken and consequently the individual cells became damped oscillators again.

We mark in Figs. 6 and S5 the parameter settings used to reproduce experimental data (see Fig. 7). Oscillator strength of $\alpha = 0.3$ and $\alpha = 0$ correspond

to wild-type and knockout mice, respectively. Coupling strength of $K = 1$ describes slice culture data well, whereas small coupling strength of $K = 0.2$ represents dispersed culture data. Since an increase of ψ from zero to 12 h deteriorates synchronization, the timing of coupling was changed from neonate ($\psi = 0$) to adult ($\psi = 1$) during the development.

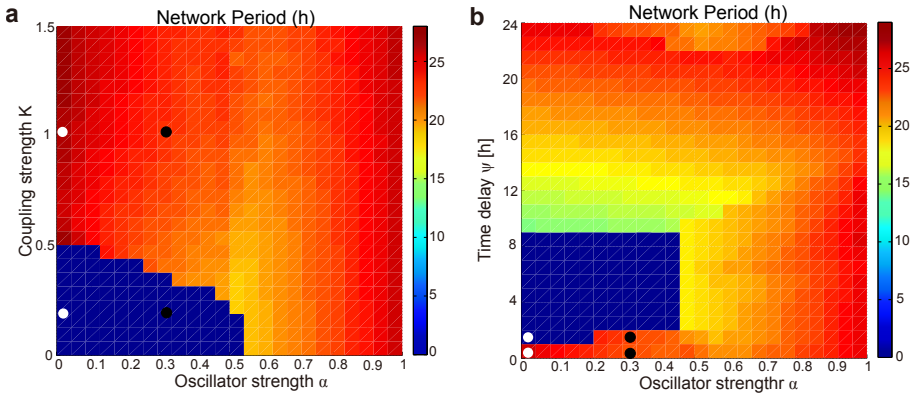

Figure S5: Oscillator network period in the simulated SCN for different choices of system parameters. **a**: Dependence of the period of the cellular network model on oscillator strength α and coupling K. The white and black points indicate conditions for simulating double knockout and wild-type mice, respectively. **b**: Dependence of the period of the cellular network model on oscillator strength α and coupling delay ψ (coupling strength was set to $K = 1$).

6 Entrainment of network dynamics to external stimuli

The entrainment region of Fig. 9 was drawn by varying the Zeitgeber intensity L_0 and Zeitgeber period T. For each combination of (L_0, T), the network (Eqs. 7-18) with external stimuli (Eq. 20) was simulated. By analyzing time series data of Y_1-variable averaged over all cells by the chi-square periodogram (significance level of 1 %) [2], period length of the cellular network was quantified. If the network period is the same as the Zeitgeber period T (difference less than 0.15 h), the network is judged to be entrained to the Zeitgeber.

7 Simulation of actograms

The actogram was drawn by simulating the network dynamics of Eqs. 7-18. At each time, the activity was evaluated by counting the number of cells, Y_1-value of which was above 70 % of its maximum. In the first 15 days of Figs. 8, *c* and *d*, the activity was plotted by applying the external stimuli of Eq. 20, which

represents the LD condition. In the following 15 days, the external stimuli were switched off to simulated the activity under DD condition. Then, to quantify the periodicity of the actogram, 5 days length of the activity data (LD data staring from the first day and DD data starting from the 16th day) was analyzed by the periodogram in Fig. S7.

To compare the network model with the experiments, behavioral rhythms in mice from both genotypes are drawn in Figs. 8, *a* and *b*, and their periods were analyzed under the same condition as those of the model in Fig. S6.

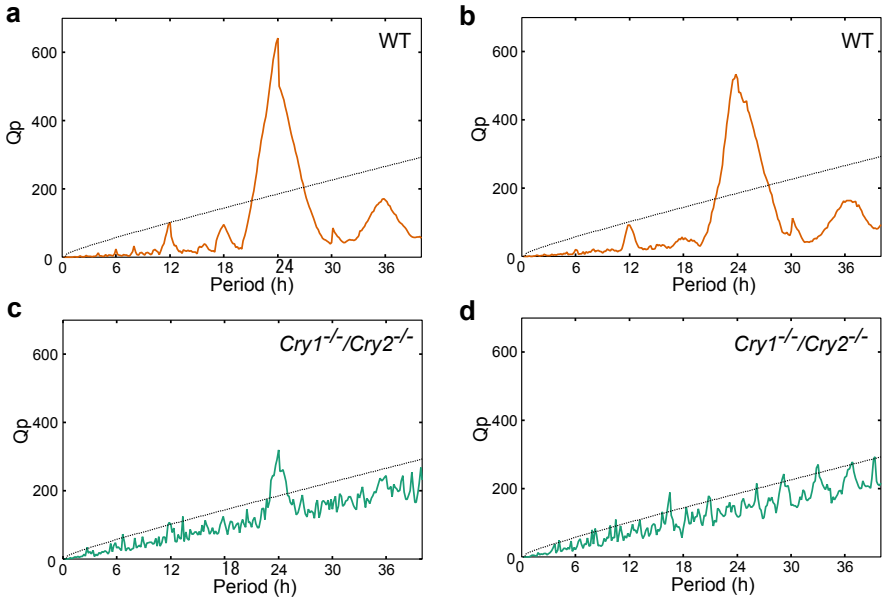

Figure S6: Analysis of behavioral period of mice across both genotypes under different lighting conditions. **a,b**: Chi-square periodogram for wild-type mouse under LD (**a**) and DD (**b**). **c,d**: Chi-square periodogram for $Cry1^{-/-}/Cry2^{-/-}$ knockout mouse under LD (**c**) and DD (**d**).

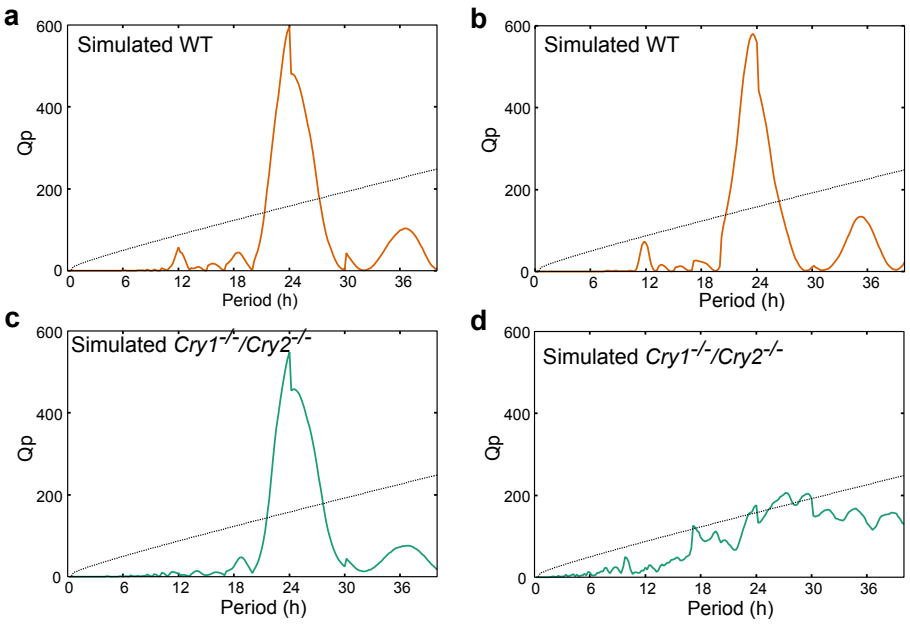

Figure S7: Analysis of period of simulated SCN from both genotypes under different lighting conditions. **a,b**: Chi-square periodogram for simulated wild-type mouse under LD (**a**) and DD (**b**). **c,d**: Chi-square periodogram for simulated knockout mouse under LD (**c**) and DD (**d**).

8 Analysis results of slice culture data

Table S1: Results of the periodicity and phase analysis for slice culture data of neonate and adult mice (both wild-type and knockout). Average and standard deviation of the period estimated by the chi-square periodogram (significance level of 1 %) [2] are indicated. Standard deviation of the phase of individual cells is represented as a quantity to measure the coherence structure. The estimated values are compared with those of the simulated network.

	Mouse	Age	Period	Phase
Experiment	Wild-type	Neonate	24.4±0.5 h	0.13 h
		Adult	25.8±2.8 h	0.64 h
	Cry1$^{-/-}$/*Cry2*$^{-/-}$	Neonate	19.0±0.2 h	0.26 h
		Adult	30.8±6.2 h	1.1 h
Model	Wild-type	Neonate	23.0±0.2 h	0.38 h
		Adult	23.9±2.7 h	0.40 h
	Cry1$^{-/-}$/*Cry2*$^{-/-}$	Neonate	26.2±0.4 h	0.10 h
		Adult	26.2±7.3 h	1.2 h

9 Parameter settings for the biochemical model

Detailed parameter settings for the biochemical model (Eqs. 7-18) simulated in the main text are summarized in the following tables.

Table S2: Two parameter settings for the biochemical model (Eqs. 7-18): (i) self-sustained oscillator (Becker-Weimann *et al.*, 2004), (ii) damped oscillator (Bernard *et al.*, 2007).

Description	Parameter	Value (Becker-Weimann, 2004)	Value (Bernard, 2007)
Hill coefficient of inhibition of Per/Cry transcription	p	8	3
Nuclear import rate of PER/CRY complex	k_{2t}	0.24 h^{-1}	0.36 h^{-1}
Maximal rate of Bmal1 transcription	v_{4b}	3.6 nM	1.0 nM
Degradation rate of Per/Cry mRNA	k_{1d}	0.12 h^{-1}	0.18 h^{-1}
Degradation rate of cytoplasmatic PER/CRY	k_{2d}	0.05 h^{-1}	0.1 h^{-1}
Degradation rate of nuclear PER/CRY complex	k_{3d}	0.12 h^{-1}	0.18 h^{-1}
Degradation rate of Bmal1 mRNA	k_{4d}	0.75 h^{-1}	1.1 h^{-1}
Degradation rate of cytoplasmatic BMAL1	k_{5d}	0.06 h^{-1}	0.09 h^{-1}
Degradation rate of nuclear BMAL1	k_{6d}	0.12 h^{-1}	0.18 h^{-1}
Degradation rate of nuclear BMAL1*	k_{7d}	0.09 h^{-1}	0.13 h^{-1}

Table S3: Parameter setting of the biochemical model.

Description	Parameter	Value
Hill coefficient of activation of Per/Cry transcription	h	2
No. of PER/CRY complex forming subunits	q	2
Hill coefficient of activation of Bmal1 transcription	r	3
Maximal rate of Per/Cry transcription	v_{1b}	9.0 nM h^{-1}
Michaelis constant of Per/Cry transcription	k_{1b}	1.0 nM
Inhibition constant of Per/Cry transcription	k_{1i}	0.56 nM
Complex formation rate of PER/CRY	k_{2b}	0.3 $h^{-1}nM^{-(q-1)}$
Nuclear export rate of the PER/CRY complex	k_{3t}	0.02 h^{-1}
Michaelis constant of Bmal1 transcription	k_{4b}	2.16 h^{-1}
Degradation rate of Bmal1 mRNA	k_{4d}	1.1 h^{-1}
Translation rate of BMAL1	k_{5b}	0.24 h^{-1}
Nuclear import rate of BMAL1	k_{5t}	0.45 h^{-1}
Nuclear export rate of BMAL1	k_{6t}	0.06 h^{-1}
Activation rate of nuclear BMAL1	k_{6a}	0.09 h^{-1}
Deactivation rate of nuclear BMAL1*	k_{7a}	0.003 h^{-1}
Production constant of transmitter	k_8	1.0 h^{-1}
Degradation rate of transmitter	k_{8d}	4.0 h^{-1}
Activation rate of coupling	k_{x1}	3.0 $h^{-1}nM^{-1}$
Total concentration of PKA	X_{1T}	15.0 nM
Degradation rate of PKA	k_{dx1}	4.0 h^{-1}
Activation rate of PKA	k_{x2}	0.25 $h^{-1}nM^{-1}$
Total concentration of CREB	X_{2T}	15.0 nM
Degradation rate of CREB	k_{dx2}	10.0 h^{-1}

10 Additional samples of bioluminescence signals

In addition to bioluminescence signals shown in Fig. 1, *a*, *b*, *d*, and *e*, six more samples are provided here for dispersed SCN cell culture of wild-type and $Cry1^{-/-}/Cry2^{-/-}$ mice. Also from simultaneous plot of the cellular signals in Fig. 5, six indivdual traces are extracted and presented for SCN slice culture of wild-type and $Cry1^{-/-}/Cry2^{-/-}$ mice (both neonate and adult).

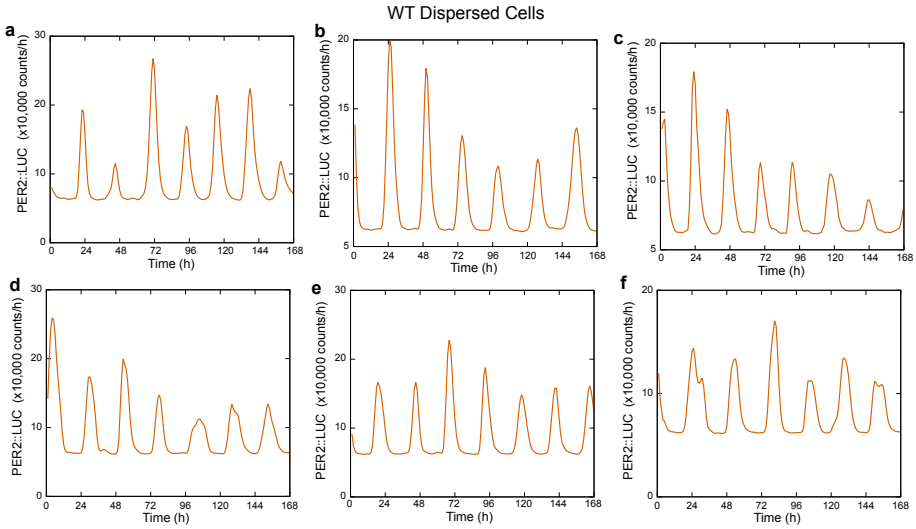

Figure S8: Six samples of bioluminescence signals recorded from dispersed SCN cell culture of wild-type mice.

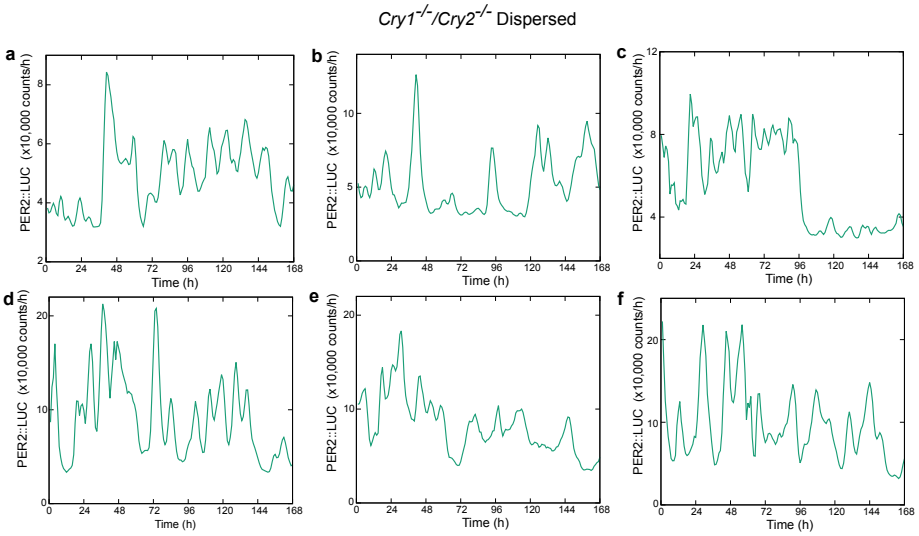

Figure S9: Six samples of bioluminescence signals recorded from dispersed SCN cell culture of $Cry1^{-/-}/Cry2^{-/-}$ mice.

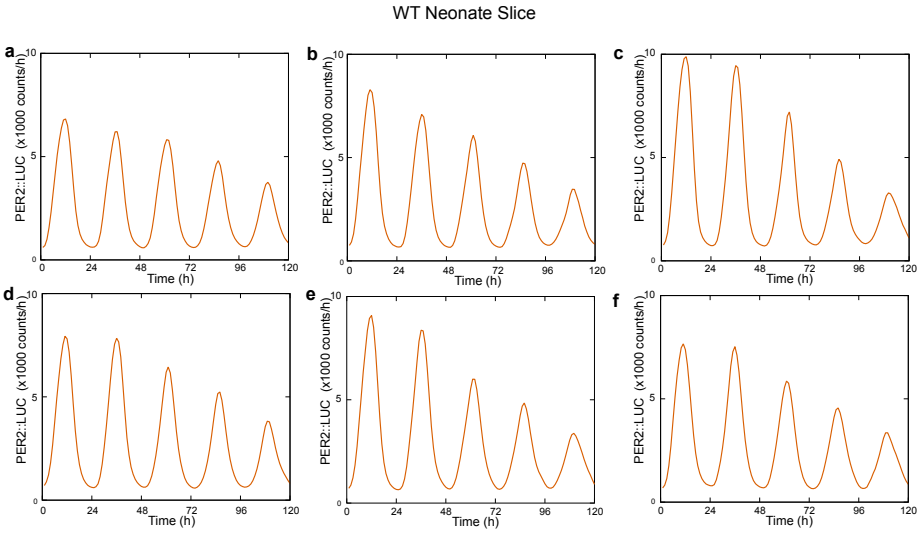

Figure S10: Six samples of bioluminescence signals recorded from SCN slice culture of WT neonate mice. From simultaneous plot of the cellular signals in Fig. 5*a*, indivdual traces are extracted in each figure.

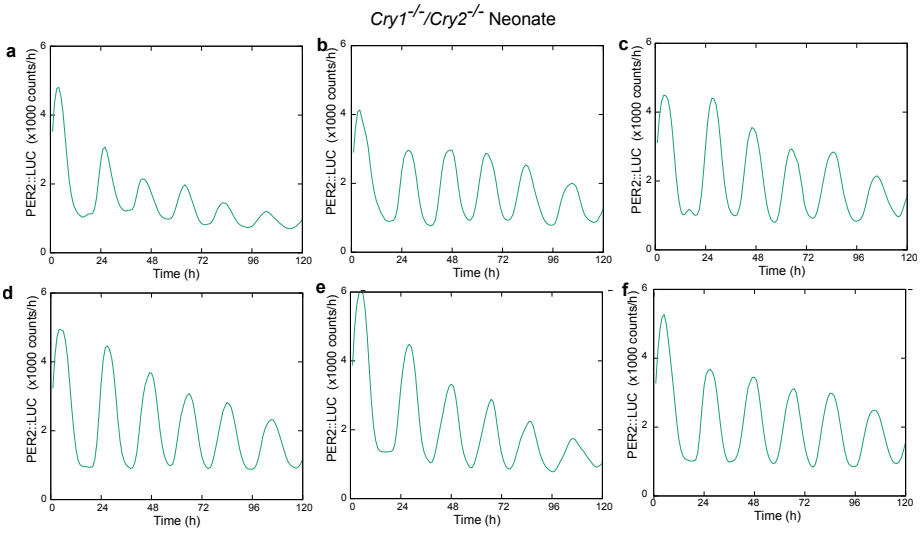

Figure S11: Six samples of bioluminescence signals recorded from SCN slice culture of $Cry1^{-/-}/Cry2^{-/-}$ neonate mice. From simultaneous plot of the cellular signals in Fig. 5*d*, indivdual traces are extracted in each figure.

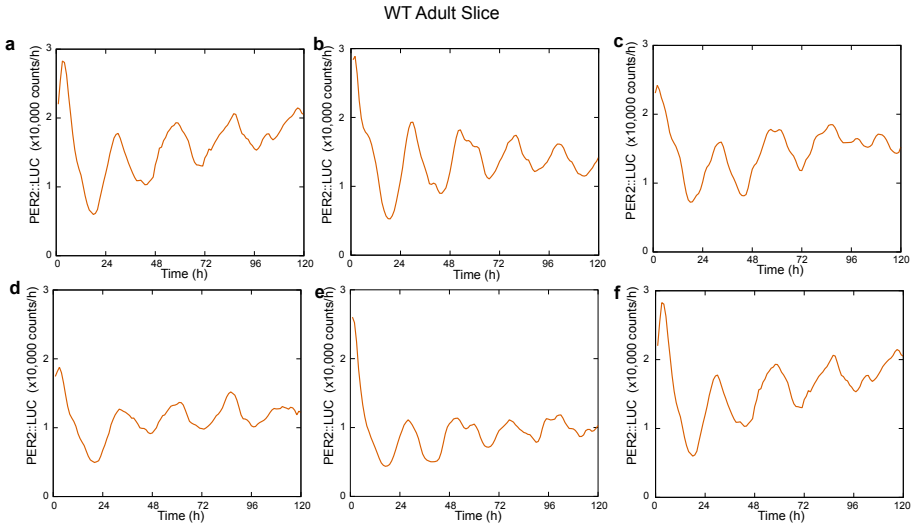

Figure S12: Six samples of bioluminescence signals recorded from SCN slice culture of WT adult mice. From simultaneous plot of the cellular signals in Fig. 5*c*, indivdual traces are extracted in each figure.

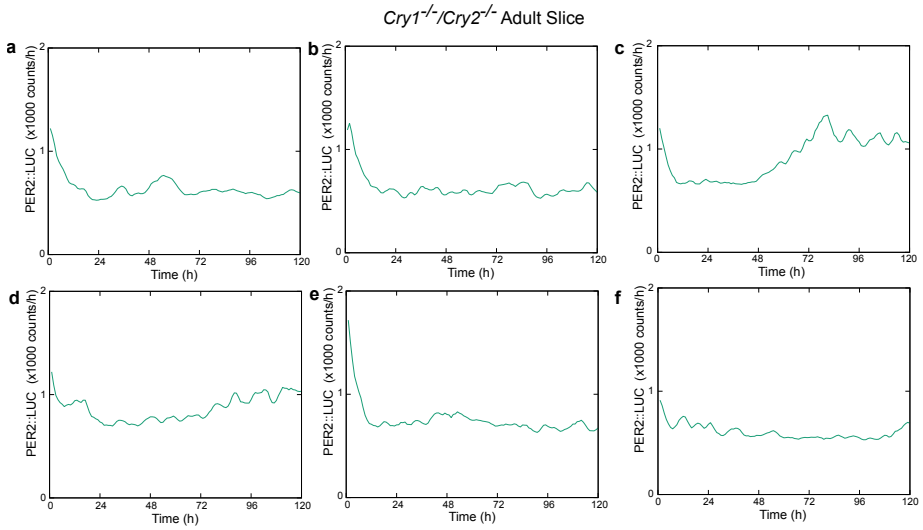

Figure S13: Six samples of bioluminescence signals recorded from SCN slice culture of $Cry1^{-/-}/Cry2^{-/-}$ adult mice. From simultaneous plot of the cellular signals in Fig. 5*e*, indivdual traces are extracted in each figure.

References

[1] Westermark, P. O., D. K. Welsh, H. Okamura, and H. Herzel, 2009. Quantification of Circadian Rhythms in Single Cells. PLoS Comput Biol 5:e1000580.

[2] Sokolove, P. G., and W. N. Bushell, 1978. The chi square periodogram: Its utility for analysis of circadian rhythms. rhythms. Journal of Theoretical Biology 72:131–160

[3] Halberg, F., Y. Tong, and E. Johnson, 1967. Circadian system phase An aspect of temporal morphology; procedures and illustrative examples. In H. von Mayersbach, editor, The Cellular Aspects of Biorhythms, Springer Berlin Heidelberg, 20–48

[4] Becker-Weimann, S., J. Wolf, H. Herzel, and A. Kramer, 2004. Modeling feedback loops of the mammalian circadian oscillator. Biophysical Journal 87:3023–3034.

[5] Bernard, S., D. Gonze, B. Čajavec, H. Herzel, and A. Kramer, 2007. Synchronization-induced rhythmicity of circadian oscillators in the suprachiasmatic nucleus. PLoS Comput Biol 3:e68.

[6] Gonze, D., S. Bernard, C. Waltermann, A. Kramer, and H. Herzel, 2005. Spontaneous synchronization of coupled circadian oscillators. Biophysical Journal 89:120–129.